Low-Radiation Cellular Inductive Powering of Rodent Wireless Brain Interfaces: Methodology and Design Guide

Nima Soltani, *Student Member, IEEE*, Miaad S. Aliroteh, *Student Member, IEEE*, M. Tariqus Salam, *Member, IEEE*, Jose Luis Perez Velazquez, and Roman Genov, *Senior Member, IEEE*

***Abstract*—This paper presents a general methodology of inductive power delivery in wireless chronic rodent electrophysiology applications. The focus is on such systems design considerations under the following key constraints: maximum power delivery under the allowable specific absorption rate (SAR), low cost and spatial scalability. The methodology includes inductive coil design considerations within a low-frequency ferrite-core-free power transfer link which includes a scalable coil-array power transmitter floor and a single-coil implanted or worn power receiver. A specific design example is presented that includes the concept of low-SAR cellular single-transmitter-coil powering through dynamic tracking of a magnet-less receiver spatial location. The transmitter coil instantaneous supply current is monitored using a small number of low-cost electronic components. A drop in its value indicates the proximity of the receiver due to the reflected impedance of the latter. Only the transmitter coil nearest to the receiver is activated. Operating at the low frequency of 1.5 MHz, the inductive powering floor delivers a maximum of 15.9 W below the IEEE C95 SAR limit, which is over three times greater than that in other recently reported designs. The power transfer efficiency of 39% and 13% at the nominal and maximum distances of 8 cm and 11 cm, respectively, is maintained.**

***Index Terms*—Automatic tracking, freely-moving electrophysiology, impedance tracking, implantable medical devices, inductive power transmission, non-ionizing radiation, rodent electrophysiology, wearable medical devices.**

I. Introduction

NEURAL INTERFACE (NI) microsystems are instrumental to physiological research and potential treatment of the nervous system pathologies such as epilepsy and Parkinson's disease. Modern NI microsystems generally perform electrophysiological neuro-monitoring and in some cases neuro-stimulation [1]. Optophysiological neural interfacing is another promising modality [2]. NI research promises discovery of new therapies for many neurological disorders, and of new ways to restore damaged neural functions.

The use of NIs in awake behaving rodent studies has become a common research technique. The technology provides a real-time view of neuronal interactions at the cellular level and of the nervous system function [3]–[6]. Research efforts to design more sophisticated NIs for rodent experiments continue to progress [7]–[9]. These experiments lead to more accurate observations of many important neurological events and ultimately to an improved understanding of the nervous system. Several practical challenges remain in the development of a small self-sufficient NI for chronic rodent studies that does not require a wired connection to bulky laboratory instruments.

Neurophysiology experiments on laboratory rodents are generally powered through cables. One problem is animal gnawing and pulling on the cables and disrupting the experiment [10]. Moreover, cables can alter the animal behavior as it has a limited sense of freedom [9]. Transcutaneous cables have also been linked to an increased risk of an infection [11]. As an alternative to cables, small-size batteries are sometimes used as a source of energy. However, the short lifetime of such batteries typically limits the length of an experiment to a few hours [12], [13]. Longer-lasting batteries are heavier and therefore do not benefit studies with small rodents such as mice and rats. As a result, long-term studies with a battery-operated NI system need to be interrupted repeatedly for conducting routine battery replacements.

Inductive powering has emerged as an attractive alternative to cables [14]. In inductive powering, air-core inductors replace the power supply cables between the device implanted in or mounted on a rodent and the rest of the experimental setup. Weakly-coupled near-field magnetic resonance technique is typically used to transfer energy wirelessly over a few centimeters distance. There are a number of recently reported innovative battery-less systems for inductive powering of implantable or wearable neural monitoring and stimulation devices for rodent electrophysiological studies [14]–[18].

In [14], a 13.6 MHz scalable rodent cage floor made of a 2-dimensional array of planar power transmitting inductive coils fabricated on a printed circuit board (PCB) is presented. A network of RFID readers detects and turns on the coil nearest to the animal implanted with or wearing an NI device. The dynamic magnetic field coverage in this design comes at the expense of

Manuscript received May 14, 2015; revised August 10, 2015 and October 29, 2015; accepted November 07, 2015. Date of publication March 04, 2016; date of current version July 26, 2016. This paper was recommended by Associate Editor S. Renaud.

N. Soltani, M. T. Salam, and R. Genov are with the Department of Electrical and Computer Engineering, University of Toronto, Toronto, ON M5R 0A3, Canada (e-mail: roman@eecg.utoronto.ca).

M. S. Aliroteh is with the Department of Electrical Engineering, Stanford University, Stanford, CA 94305 USA (e-mail: miaad@stanford.edu).

J. L. Perez Velazquez is with the Brain and Behaviour Centre, Division of Neurology, University of Toronto, Toronto, ON M5P 4A2, Canada.

Color versions of one or more of the figures in this paper are available online at http://ieeexplore.ieee.org.

Digital Object Identifier 10.1109/TBCAS.2015.2502840

one set of costly hardware (i.e., an Ethernet adapter, a microprocessor, a magnetic sensor, and an RFID reader) for every three coils in the array.

In another design [15] (also operating at 13.6 MHz), all coils in the cage floor array are connected in parallel. The induced power shifts naturally toward the coil directly below the animal-mounted NI power-receiving coil. This is due to that power transmitting coil having a lower equivalent parallel resistance than that of the other, non-loaded coils in the array. The simplified tracking technique in this design comes at the cost of increased power loss in the power transmitter, by a factor of approximately the number of coils in the array.

In [16] and [17] the array is replaced by a single power transmitting coil operating at 8 MHz. A mechanical X-Y stage table is used to adjust the placement of the power transmitting coil with respect to the receiver coil. However, the power lost in the moving mechanical parts and the complexity of the mechanics is a limitation.

A lower-frequency (120 kHz) inductive link is reported in [18]. Copper-wound ferrite core (receiver) is powered with a commercial transmitter. The choice of the low operating frequency increases the level of the transferable power due to the higher allowed magnetic field safety limit at lower frequencies [23]. However, the use of a ferrite core as the receiver limits the delivered power (0.5 W at the allowed magnetic field limit of 160 A/m) [22].

The designs in [14]–[18] rely on the maximum energy transfer efficiency principle for the design optimization. This principle, however, does not include a key practical (and regulatory) design constraint for implantable and wearable biomedical devices which is to deliver the maximum energy to the load with respect to the maximum allowed magnetic field (non-ionizing radiation) level. In wireless electrophysiology experiments, the key design objective for an inductive powering system is delivering the highest energy to a small-size receiver (RX) (either implanted or worn). The maximum power transferable to the receiver is limited among other things by: (a) the maximum receiver size, and, importantly, (b) the maximum level of magnetic field intensity considered safe.

The safe radiation level is quantified by the specific absorption rate (SAR) limit which for humans is governed by IEEE C95 standard [23] and by country-specific health regulatory bodies such as the Food and Drug Administration in the USA. The receiver needs to be large enough to harvest sufficient power from a magnetic field with an intensity below the regulated SAR limit of $f/16.3$ MHz [23] but small enough to be implanted or worn. Maintaining a SAR level much (i.e., a factor of 5 or more) lower than the limits defined in [23] is particularly important in rodent electrophysiology experiments. This is because the non-ionizing radiation absorbed by an animal can cause more severe physiological and behavioral effects due the animals having a less efficient thermoregulatory system than humans [24]–[26].

Compared to operating at higher frequencies, operating at a lower-MHz frequency, a transmitter can deliver more power within the SAR limits, despite being less energy-efficient. This is because the allowable density of the magnetic flux is increasingly higher at the lower MHz frequencies [23]. Continuing this trend, theoretically, even more power can be delivered at even lower frequencies. However, making coils resonant at below-1 MHz frequencies requires ferrite-core inductors (as in [18]) which makes the receiver excessively heavy and lossy.

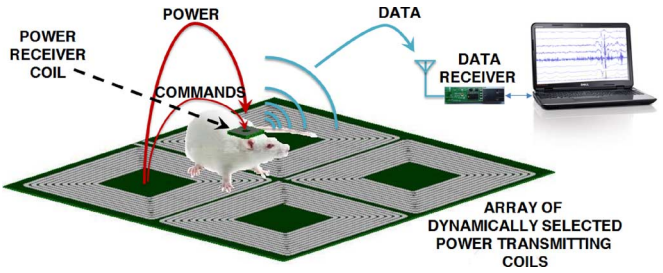

Fig. 1. Envisioned experimental setup for inductive powering and data communication in chronic experiments with freely moving rodents.

This paper presents a methodology and design guide for low-specific-absorption-rate (SAR) inductive powering of batteryless NI microsystems implanted in or mounted on laboratory rodents. The paper extends on an earlier report of the principle and demonstration in [27], and offers a more detailed methodology of the design and additional experimental results characterizing the system implementation and the power delivery performance. As shown in Fig. 1, the inductive powering system consists of an array of planar power transmitting coils located at the bottom of the cage. The system dynamically tracks the animal and turns on the nearest coil. Neural recording data can be transmitted to a nearby computer while commands can be communicated over the same inductive link used to power the device. Compared with the previously reported systems in [14]–[18], the design offers: (a) a lower operating frequency of 1.5 MHz (without the use of ferrite cores) which results in a higher transfered-power-to-SAR ratio, (b) a cost-effective and more power efficient impedance tracking technique to locate the transmitter coil nearest to the animal by monitoring the current each neighboring TX coil draws from the power supply via its power amplifier, and (c) a distinctly higher scalability and lower overall cost by employing much fewer expensive components as compared to the design in [14]. Such a powering solution has the potential to become an essential tool for many *in vivo* rodent experiments.

The rest of the paper is organized as follows: Section II describes the optimization rationale and the steps to design the RX and TX coils. Section III presents an implementation of the proposed system including the impedance tracking. Section IV discusses the experimental measurement results (including the load tracking and automatic tuning functions), and compares the system performance with existing designs.

II. Methodology: Coils Design

A. General Considerations

The transmitting (TX) and receiving (RX) coils are fabricated on printed circuit boards (PCB) (with 4 oz copper layers in this design). Fig. 2 shows the layout parameters of a square PCB spiral coil, which is the geometry selected here for both the TX and RX coils for simplicity. Depending on the geometry of the microsystem, a differently shaped RX such as octagonal or

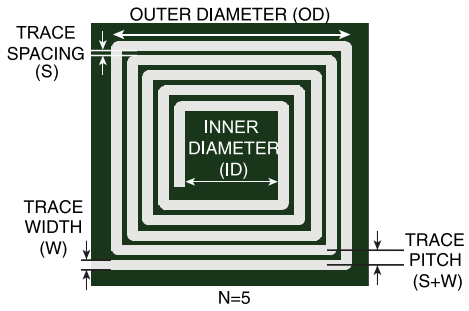

Fig. 2. Main layout parameters of a square spiral inductor fabricated on a 2-layer printed circuit board. The inner diameter (ID), outer diameter (OD), and trace width (W) are the main design parameters of a planar spiral inductor. Turn spacing (S) is often as small as possible as the operating frequency is much smaller than the coil self-resonant frequency. The number of turns (N) is calculated once the other four parameters have been defined.

round may be more area-efficient. However, since the RX has not been designed here for any particular microsystem, no particular shape was found more suitable. The coil traces are fabricated on the top layer, while the bottom layer is reserved for the return path. The main layout parameters of the square spiral coil, shown in Fig. 2, are the inner diameter (ID), the outer diameter (OD), and the trace width (W). The minimum trace spacing (S) is constrained by the PCB fabrication process due to the low operating frequency [28]. The number of turns (N) is a function of the above parameters since geometrically: $OD = 2NW + (2N - 1)S + ID$.

Both the TX and RX coils in this design are operated far below their self-resonant frequency (f_{SRF}), so the parasitic turn-to-turn capacitances do not impact the quality factor or the resonant frequency [28]. Therefore the best value for S is the minimum trace spacing of the fabrication process. The choice of OD for the TX is determined based on the separation distance between the TX and the RX coils. The choice of RX OD, on the other hand, is based on a design trade-off between the microsystem size and its power transfer efficiency. The impact of the the inner diameter (ID) on the quality factor and the coupling coefficient is less than that of the outer diameter. Even though a small ID typically leads to a better quality factor, a zero TX coil ID is often not optimal. This is because the turns of the coil near the center do not contribute significantly to the inductance value despite still significantly increasing the parasitic resistance [30].

B. RX Coil

Based on the analysis provided in [28], [30], [31], maximizing both coils quality factors results in the highest achievable power transfer efficiency. In a power-efficient design, the individual quality factor of each coil must be comparable to $1/k$ (where k is the coupling coefficient) with the product of the two being significantly larger than $1/k^2$ (based on the derived efficiency expression in [28], [30], [31]). In a wireless electrophysiology system, the quality factor of the RX coil is far more limited than that of the TX coil. This is due to the size constraints imposed by the maximum dimensions of the implant or the wearable device. The RX size is therefore the most limiting factor in determining the overall power transfer efficiency.

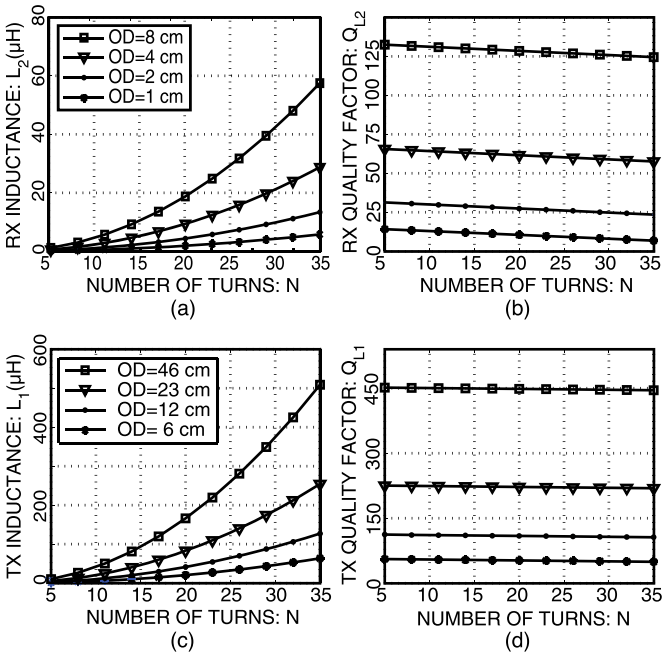

Fig. 3. RX [(a) and (b)], and TX [(c) and (d)] coils inductance and quality factors. Planar rectangular coils with different number of turns (N) and outer diameters (OD) are simulated at the 1.5 MHz operating frequency. The coil structures are designed on a 2-layer PCB substrate with 4 oz copper thickness and dielectric thickness of 0.3 mm. The coil quality factors are improved linearly by the increase in OD, but drop slightly with more turns since the coil resistance grows faster than its inductance as the gaps between traces takes up more of the trace pitch (center-to-center distance between 2 adjacent turns) with each added turn. The expected quality factor of the receiving coil can be estimated based on the plots in (b). The TX quality factor can be estimated based on the plots in (d) once RX size is determined.

Fig. 3(a) and (b) show the inductance and the quality factor, respectively, of RX coils with different outer sizes (OD) and number of turns (N) simulated at 1.5 MHz operating frequency, as motivated for in Section I. Evidently, for a fixed OD, a greater N does not significantly impact the component quality factor (Q_{L2}) despite sharply increasing the inductance of the coil. Therefore, regardless of the number of turns, the power transfer efficiency is limited by the outer diameter of the receiver.

While the number of turns (N) does not control the quality factor of the RX coil, it does determine the optimum value of the source and load resistances (R_S and R_L), which result in the best impedance matching and power transfer efficiency. Based on the 2-port model in [31], the real part of the output impedance of the receiver coil is given by $R_{21} = k^2 Q_1 \omega L_2$, where k is the coupling coefficient, Q_1 is the quality factor of transmitting coil and L_2 is the inductance of the receiver. For the best matching of RX coil to the load, N must be selected such that ωL_2 is equal to the geometric mean of R_{21} and R_L [38]. Based on the size of the rodent in the target animal experiment (white Wistar rat), an OD of 4 cm is selected for the receiving coil. An N of 11 is selected to match the RX to a 3.3 kΩ load at the operating frequency of 1.5 MHz. Based on the RX OD, and the average and maximum animal heights of 8 cm and 11 cm (when walking and standing up respectively),

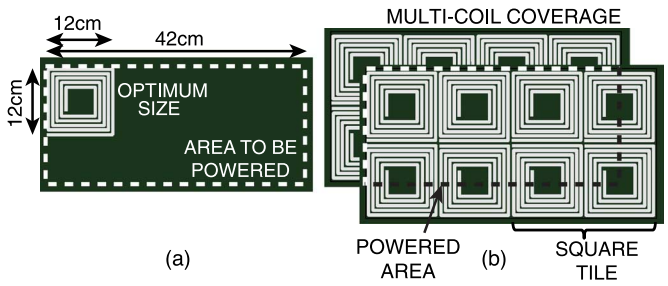

Fig. 4. (a) An optimally sized TX coil which is smaller than the required coverage area to be powered. (b) An array of optimally-sized TX coils designed to cover the cage floor area (the implemented multi-coil technique). The array has two layers of overlapping coils shifted by 50% of their outer diameter for more uniform magnetic field coverage and eliminating dead spots where delivered power is too low.

the average and minimum coupling coefficients of 0.15 and 0.07 are expected.

C. TX Coil

Fig. 3(c) and (d) show the inductance the and quality factor of the transmitting coils, where the ID is selected to be nearly 30% of the OD (which yields approximately the best quality factor at the given frequency based on a field simulation with FastHenry solver). It is evident that, similar to the RX coil, the TX coil quality factor improves only by increasing its OD. Unlike the RX, however, the TX is stationary and does not have any particular size limitations. Nonetheless, the TX must be large enough: (a) to cover the entire area where the receiver could be located, and (b) to create the highest possible coupling coefficient k at the expected coil separation distance d. While the coupling coefficient k is already limited by the size of RX, the TX coil should be large enough not to further diminish the k at the operating distance d.

It is known that there is a single optimum TX diameter for every given RX-TX separation distance [30] (this is also verified here by the field simulation results in Section II-D). Based on the same analysis, the expected optimum values of TX OD are loosely proportional to the RX-TX separation distance d. TX sizes that are several times greater than d, create excessive non-ionizing radiation (due to elevated field intensities). TX coil dimensions smaller than this value, on the other hand, will result in an impractically small k leading to a much degraded efficiency value. Therefore, based on the expected separation distance d of 8 cm, a TX OD of 12 cm is selected which according to Fig. 5(c) and (d) minimize the radiation level without diminishing k.

D. Multi-Coil TX Array

While the optimal TX coil OD of approximately 12 cm achieves the best inductive coupling-to-radiation ratio, it may not be necessarily large enough to cover the entire area that needs to be powered [as shown in Fig. 4(a)]. The area to be powered in this design is the 42 cm × 18 cm footprint of an animal cage. The area of the optimum TX, however, is much smaller than this area [see Fig. 4(a)]. The solution is to cover the cage floor area by a multi-coil array [14] of optimally-sized coils as shown in Fig. 4(b). Two overlapping arrays of 12 cm × 12 cm TX coils are designed to power an overall floor area of 40 cm × 18 cm. Within this area, only the TX coil nearest to the receiver will be turned on at any given time. The 50% overlap in both X and Y directions eliminates dead spots.

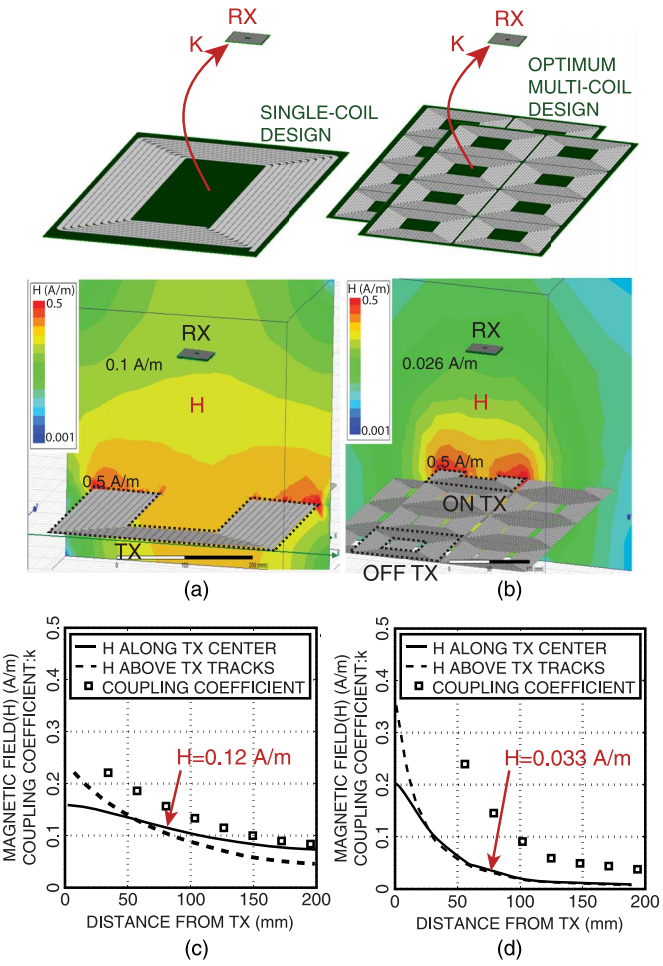

Fig. 5. Magnetic field simulation results of (a) a single large coil transmitter versus (b) array of optimally sized TX coils for equal current of 1 A flowing through both coils. (c) Plotted values of H field and coupling coefficient (k) along the center and above the tracks of the single large coil, and (d) the multi-TX floor.

The magnetic field simulation plots in Fig. 5(a) and (b) demonstrate how an array of optimally-sized transmitting coils [Fig. 5(b)] results in a significantly lower non-ionizing radiation (magnetic field intensity) level than that of a single large coil in Fig. 5(a) (0.026 A/m versus 0.1 A/m). This result validates the need for the more complex multi-coil technique.

One drawback of the multi-coil techniques is the higher levels of the magnetic field strength within a few millimeters of the floor directly above it. This problem is easily mitigated by creating a small gap between the surface of the coils and the cage bottom which is done in this design by placing a 5 mm PMMA (plexiglas) layer over the transmitting coils.

The field simulation results in Fig. 5(c) show how the coupling coefficient changes as the RX moves away from the center of the large TX coil that covers the whole floor, orthogonally to it. Fig. 5(d) shows how the optimally-sized TX coil provides the same or greater k at the distances less than the nominal separation distance of 8 cm.

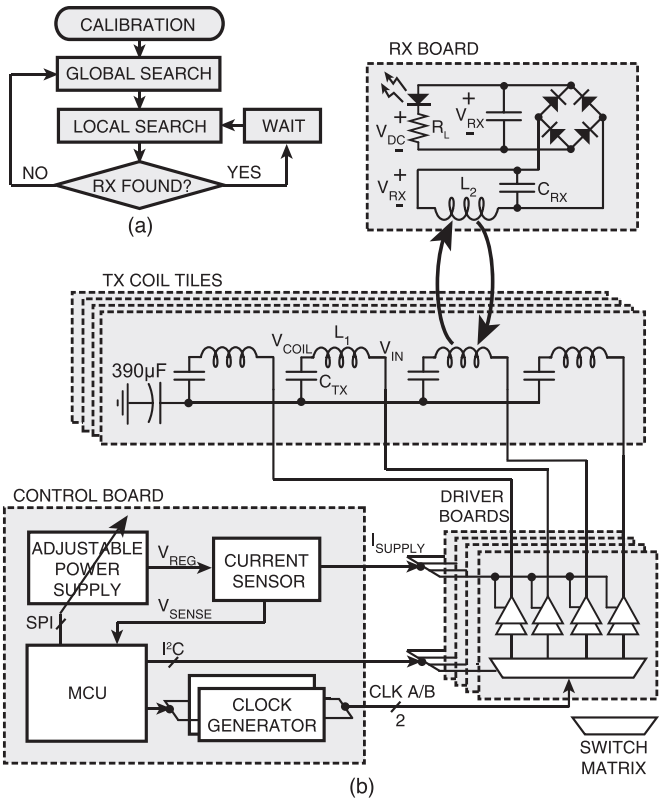

Fig. 6. (a) The principle of operation of the multi-coil powering system (as executed by the MCU algorithm), and (b) the schematic diagram of the multi-coil system including the RX board, and the TX system comprised of the tiles, the drivers and the control unit.

III. Design Guide: Multi-Coil Powering System

A. System Architecture

The principle of operation of the inductive powering system is illustrated in Fig. 6(a). The algorithm routinely searches for the TX coil nearest to the RX, and powers that coil only.

Fig. 6(b) shows the schematic diagram of the system. It is comprised of the RX board and the three types boards within the transmitter. As shown in Fig. 6(b), the receiver board consists of the coil, resonating capacitor C_{RX}, a bridge rectifier, a resistive load, and an LED to indicate successful inductive power transfer to the RX. The TX includes the TX tiles, the driver boards, one per tile, and the single control unit. The drive board pairs each of the four coils in a TX tile with a dedicated power amplifier (PA). The control unit consists of a microcontroller (MCU), a variable voltage supply, and a current sensing differential amplifier to indicate the level of current drawn from the power supply by each PA. The variable supply and the driver boards are all controlled by the MCU.

B. Tiles

As shown in Fig. 5(b) and in the functional block diagram of the cellular powering system in Fig. 6(b), the TX array is organized into "tiles" for scalability. Each of the four tiles consists of four coils connected to a single driver module. Although each of the four coils in a tile are routed to a separate amplifier, having all four drivers on a single board reduces the fabrication and assembly cost. This is because all four amplifiers are routed to the power rails and the I2C bus via the same vertical connector. The driver module docks with one TX tile and drives one of the four coils in the tile based on a command sent from the MCU. The command is sent over an I^2C bus routed to the driver board located in the center of the tile, under it. TX tiles are laid side-by-side to provide the desired coverage without a need for additional wiring.

C. Driver Modules

As shown in Fig. 6(b), the driver modules tap onto the bus lines routed within TX tiles in order to get power from the supply buses, and commands from the MCU. A frequency-tuned 1.5 MHz square wave signal is routed to each driver board at the input of the dual switch matrix (ADG729) on the board. The square wave activates one of the coils in the tile when the driver board is selected by the MCU. The switch matrix powers the selected coil by routing the CLK A/B signal to the input of the corresponding 2-stage driver. CLK A and CLK B buses carry the same square wave signal but with overlapping coil-connect and coil-disconnect times to ensure smooth transitions when disconnecting one coil and connecting the next.

The first stage of the driver circuit is an adaptive preamplifier (L6741) which drives the gates of an NMOS class AB stage (DMN4031). The adaptive loop in the preamplifer monitors the DC level at the output of the second stage and adjusts the DC biasing voltages in the first stage to minimize the DC shunt current between the supply and the ground under various loading conditions.

D. Control Board

As also shown in Fig. 6(b), the single control board consists of the MCU (MEGA A3BU), voltage supplies and the current sensing circuit. There are 2 power supplies on the control board: a variable supply (not shown) controlled by the MCU which powers all the PAs on the driver boards, and a fixed supply which powers all other circuits in the transmitting system.

As described by Fig. 6(a), the MCU algorithm works in one of the following three states: (1) calibration which runs at power-up, when the MCU determines the resonant frequency and the equivalent series resistance of each coil, (2) a local search to find the coil nearest to the receiver by tracking the impedance of each of the eight coils near the last known position of the receiver using the "current sensing feedback" [see Fig. 6(b)], and (3) a global search which only runs when the local search is not successful. The global search scans all the coils across the floor to find the one with the highest impedance drop. The global search is also performed once after the calibration is complete to determine the position of the load initially.

E. Cellular Powering by Load Tracking

To turn on the nearest coil to the receiver, the control unit must track the location of the closest coil to the RX. A common technique for RX coil localization is to use static magnetic sensors [14], [17] to sense a permanent magnet attached to the RX. Another technique is to use a third coil to sense the proximity

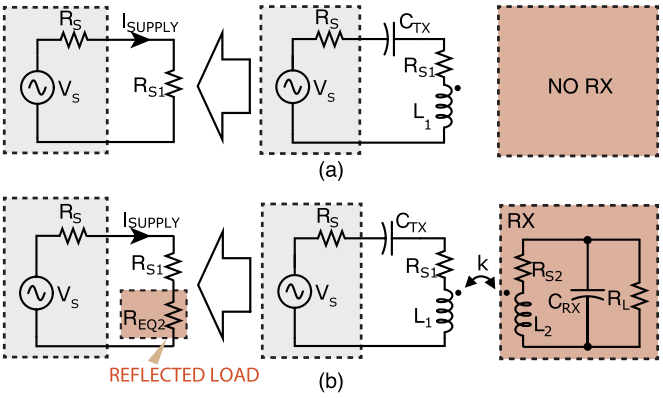

Fig. 7. Load tracking technique to locate the RX based on the mutual loading effect of the RX on the nearest TX coil. (a) When there is no RX present, I_{SUPPLY} current is at its maximum. (b) When an RX is near a TX coil, I_{SUPPLY} reduces (and thus the signal V_{SENSE} in Fig. 6(b) drops due to the added impedance R_{EQ2}).

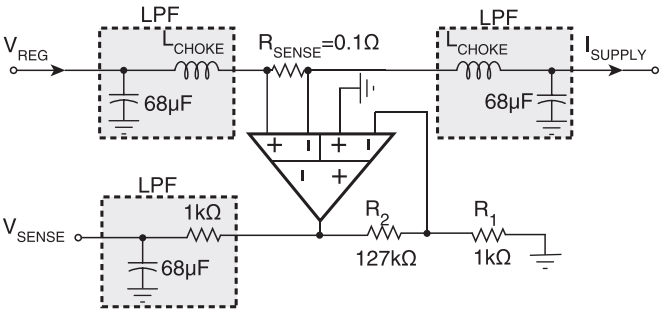

Fig. 8. Amplifier circuit to read the supply current level while the tracking scans through all the transmitting coils. High frequency reject components are used at inputs and outputs to improve sensing SNR.

of the RX by sensing the change it creates in the resonance frequency of the third coil [19]. It is possible, however, to sense the presence of the receiver without using such additional components by measuring the impedance of the transmitting coil terminals. Fig. 7 shows how the presence of the receiver [Fig. 7(b)] will impact the total impedance looking into the transmitting coil terminals. The added "reflected impedance" R_{EQ2} appears in series with the equivalent series resistance of the coil R_{S1} causing a lower current being drawn from the supply as compared with the case when no receiver is present [Fig. 7(a)]. The microcontroller scans through all the transmitting coils and records the impedance of each coil by sensing the current drawn from the supply. By comparing the measured value of the impedance with the value recorded during the calibration phase, the controller identifies the coil with the most impedance change as the one nearest to the RX.

Fig. 8 shows the impedance sensing circuit that monitors the level of the current I_{SUPPLY} drawn from the voltage supply V_{REG}. The supply current is passed through a small 0.1 Ω sense resistor which creates a voltage drop that is amplified by the differential difference amplifier (EL8172) to generate the output voltage V_{SENSE}. LC low-pass filters with high-frequency rejecting chokes (L_{CHOKE}) and an RC low-pass filter are placed at the inputs and output of the amplifier, respectively. This is done to improve the inband sensing SNR as the sensing signal level can be very small when the RX is farther away from the TX. An analog-to-digital converter on the controller board reads

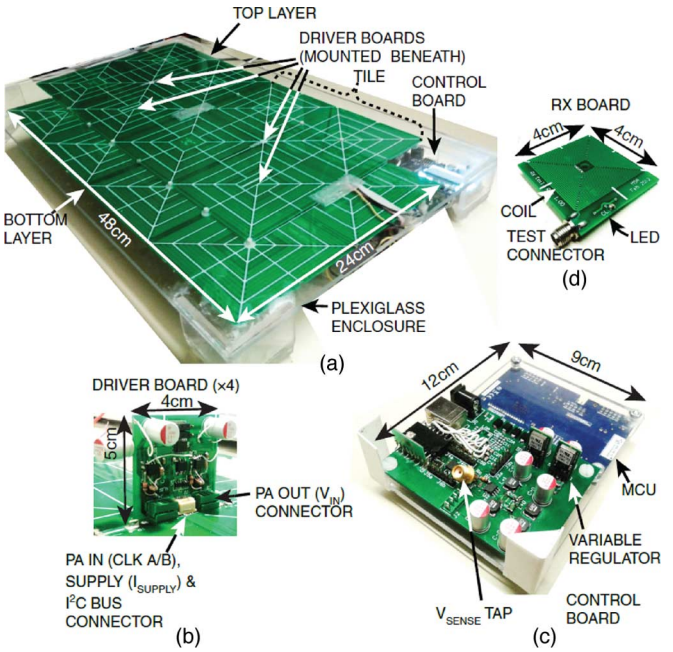

Fig. 9. (a) Working prototype of the cellular inductive powering system with the control board in the upper right corner. (b) One of the four driver boards plugged into the back of the TX tiles. (c) Control board consisting of an Atmel XMEGA A3BU board and a custom board housing power supplies, the current sensing circuit, clock generators, and buffers. (d) Receiver board consisting of a coil, a rectifier, a load and the LED.

the output signal of the differential difference amplifier in Fig. 8 and sends it to the MCU. A moving average loop in the MCU code further rejects high-frequency artifacts on the V_{SENSE} for more accurate coil selection.

IV. Results

A. Fabricated Prototype

Fig. 9 shows the working prototype of the powering system fabricated on 4 oz copper PCB substrates. The floor [Fig. 9(a)] is powered by 4 driver boards mounted beneath the coil array [displayed individually in Fig. 9(b)]. The control board [shown in Fig. 9(c)] calibrates all 16 coils one at a time to individually determine their resonant frequencies.

After the calibration, the RX board [shown in Fig. 9(d)] is powered inductively when it is held above any of the TX coils in the array. There is a small (500 msec) delay before the RX is powered for the first time as the system goes through a global search. After the first global search, the algorithm goes into the tracking mode where the search is much faster (125 msec), since only the neighboring coils are evaluated. The RX LED flashes during the search but is solid when the RX is found and power is delivered continuously. A 200 mF supercapacitor keeps the output voltage of the RX steady during the search periods. It can hold the rectified voltage within 100 mV of its initial value (before the RX power is disconnected) for about 3.3 seconds.

B. Transient Measurements

The measured TX transient signal waveforms at various points along the power transmission path are displayed in Fig. 10. CLK A/B is the frequency-calibrated signal from the

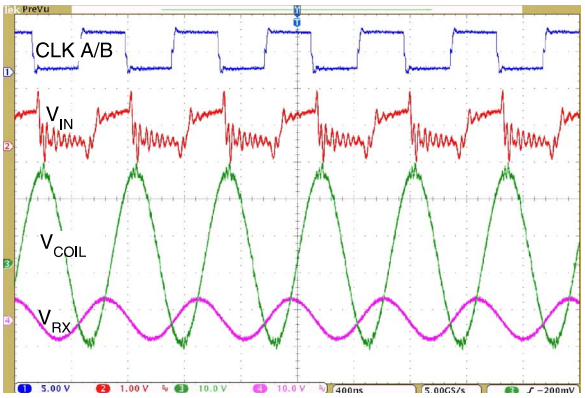

Fig. 10. Experimentally measured transient signals of the powering system at various nodes along the signal distribution path. CLK A/B is the frequency-calibrated signal generated by the MCU, V_{IN} is the output signal of the amplifier driving a TX coil at resonance. V_{IN} is attenuated due to the low equivalent resistance of the series resonant tank. V_{COIL} is the high-voltage swing at the center node of the TX resonator (between coil and the capacitor C_{TX}), and V_{RX} is the voltage induced in the receiver.

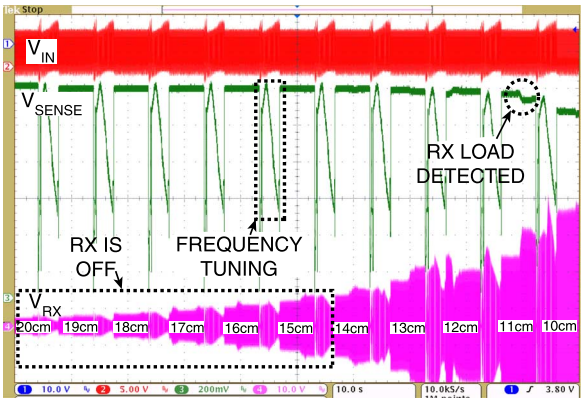

Fig. 11. Experimentally measured signal levels induced in the receiver when it is positioned at different distances from the transmitter (20 cm down to 10 cm). The impedance sensing voltage V_{SENSE} drops significantly below 12 cm indicating proximity of the receiver to the transmitter.

MCU board fed into the input of the driver boards. V_{IN} is the output of a driver board fed to the input terminal of a transmitting coil. V_{COIL} is the high-voltage swing of the resonating node between the coil and the series capacitor C_{TX} [Fig. 6(b)]. V_{RX} is the induced voltage in the receiver at the resonating node as shown in Fig. 6(b). The square wave signal V_{IN} is partially attenuated as it drives a very low-impedance load, which is the equivalent series resistance of the transmitting coil in series with C_{TX} at resonance.

The received signal levels are shown in Fig. 11, where the RX board is positioned at various distances from the TX coil starting from 20 cm, and moving closer to the transmitting coil by 1 cm each step. Repeated dynamic tuning intervals occur while the receiver is moving closer to the floor in Fig. 11. The receiver is off until the 14 cm proximity point since the signal level in the receiver is not strong enough to turn on the bridge rectifier prior to that point. After the receiver turns on, the flat region of the transmitter impedance sensing voltage (V_{SENSE}) waveform starts to drop slowly. Once the drop in V_{SENSE} is large enough, it is detected by the ADC and the MCU algorithm. As evident from the V_{SENSE} waveform in Fig. 11, that point is

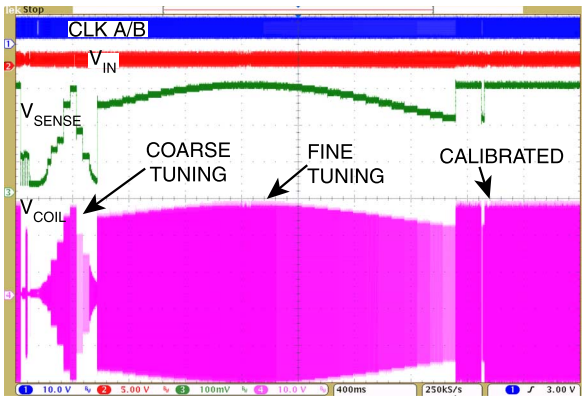

Fig. 12. Experimentally measured resonance tuning waveforms during the calibration period which runs at the startup. The calibration algorithm finds the resonance frequency and the series resistance of each coil (without a receiver present). The supply current sensing voltage, V_{SENSE}, indicates the equivalent series conductance of each coil. The algorithm finds the best frequency range (coarse tune), then finds the best point within that range (fine tune).

when the receiver is at 11 cm or closer to the transmitter. Farther than 11 cm, the drop in the V_{SENSE} voltage is not large enough for the MCU to reliably detect its presence.

C. Frequency Calibration

Upon a startup the system goes into the frequency calibration phase. The goal is to find the exact resonant frequency and equivalent series resistance of each coil, which will later be used to individually tune the TX coils and track the RX coil, respectively. Without frequency calibration, there will likely be an unwanted reactance in loop of the transmitter circuit in Fig. 7(b)(left) as the exact resonant frequency of each TX coil can be slightly different from the expected value with which the coil is initially driven. This additional reactance causes a reduction in the delivered power as well as the maximum distance at which the receiver is detectable with the scheme in Fig. 7(a), (b). While implementing a similar algorithm at the RX could further increase the detection sensitivity, it may not be practical as the power to run the algorithm would need to be sourced from the power harvested at the RX. In addition to possibly being counter-productive, RX tuning is less significant as the RX quality factor is a few times smaller than the TX one in this design, which makes R_{EQ2} in Fig. 7(b) a weaker function of the RX frequency mismatch, as compared with the TX.

Fig. 12 shows the transient performance of the system during calibration, where the frequency response of each of the 16 TX coils is evaluated to determine their resonant frequency. The transient waveforms of the impedance sensor, V_{SENSE}, and the resonating node, V_{COIL}, during calibration are shown in Fig. 12.

The MCU first sweeps the frequency of the driving signal (CLK A/B) over a wide range of frequencies from 500 kHz to 2 MHz, in 10 coarse steps, for each TX coil. Each coil is then fine-tuned with smaller frequency increments (50 kHz at a time) within the previously determined subrange of the best impedance score to find the exact resonance frequency of each individual transmitter. The coarse tuning is to accommodate a variety of coil sizes and geometries that may need to be operated

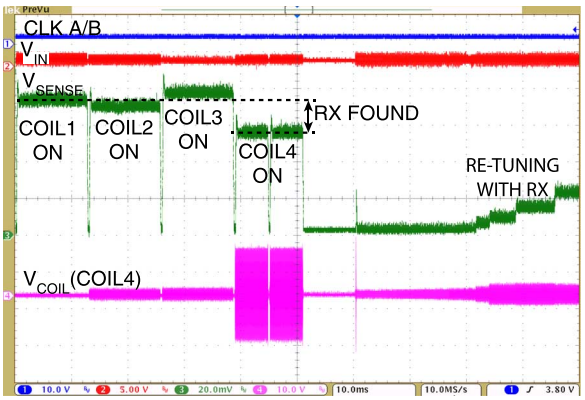

Fig. 13. Experimentally measured waveforms of the system in the tracking mode. During the calibration phase, the average value of V_{SENSE} is recorded after driving each TX coil at its resonant frequency point. The coil whose current impedance varies the most from its value pre-recorded during calibration (here it is COIL 4) is the one closest to the receiver.

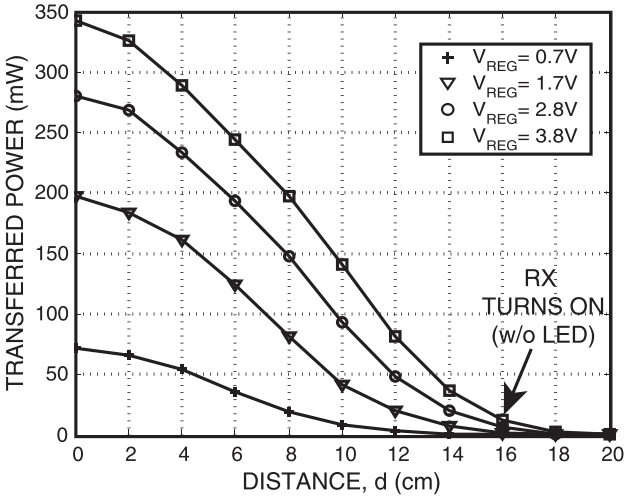

Fig. 14. Experimentally measured receiver output power level (after rectification) at 0–20 cm vertical distances from the TX tiles for four different supply voltage settings.

at a different frequency within the 500 kHz–2 MHz frequency range. Although the coarse tuning searches over a 1.5 MHz frequency range, the actual frequency variation among TX coils is a fraction of that [<10% as shown in Fig. 17(a)]. In this design, the fine-tuning (in Fig. 12) is the routine which compensates for the coil-to-coil resonance frequency variations within the array.

In Fig. 12, the inverse of the sensed signal V_{SENSE} indicates the equivalent series resistance (ESR) of the coil which is minimized at the resonance point. The minimum sensed ESR is equal to $R_{S1} + R_S$ as shown in Fig. 7(a), where R_S is the power amplifier output impedance, and R_{S1} is the winding resistance of the coil. After calibration, the exact resonant frequency and ESR of all 16 coils are stored in the MCU memory, and are later used to continuously find and activate the best TX coil (in the load tracking mode).

D. Load Tracking

After the calibration, the MCU algorithm performs a global search during which each coil is driven by a signal of its resonant frequency which was recorded during the calibration phase. The MCU records the impedance score of each TX coil again during a global search and compares them with the ones initially measured during calibration. The coil whose impedance deviates the most from its calibrated value is selected for powering.

After the global search, the controller goes into the tracking mode whereby the algorithm routinely checks the impedance of the neighboring coils to determine if any of them have a higher impedance deviation score than that of the current coil. At that point, the MCU switches to the better scoring coil.

Fig. 13 shows the variations of V_{SENSE} and the coil voltage during the last four steps of the local search (tracking). The receiver is at an approximately 10 cm distance from the nearest TX coil ("COIL 4" in this screenshot). As seen here, the impedance sensing voltage V_{SENSE} drops by more than 10 mV below that of the other coils. This clearly indicates the presence of the receiver. In the measurement setup of Fig. 13, the oscilloscope channel 4 probe is connected to the input node of COIL 4, which is why there is no signal when COILs 1–3 are being powered. The small variations in the V_{SENSE} while driving the other 3 coils is mainly due to the different placement of the other coils with respect to the receiver and each other, as well as other TX coils in the array. All the impedance variations that are not a result of the RX proximity are removed when calculating the impedance change as the algorithm subtracts the current score from the unloaded score recorded during the calibration phase. The originally calculated scores during calibration contain all the coil-to-coil variations that are not a result of RX proximity. Therefore subtracting them from the loaded values leaves only the impact of the RX.

E. Power Transfer Measurements

The measured levels of the transferred power versus the RX-TX distance varying between 0 and 20 cm are plotted in Fig. 14, for four different power supply voltage settings. The indicator LED in Fig. 6 has been removed for improved RX sensitivity. The supply voltage is determined by a digitally adjustable power supply controlled by the MCU over an SPI interface as shown in the Fig. 6. The system runs at the nominal setting of 2.8 V during normal operation. The supply setting is adjusted based on the maximum operating distance at which the system is expected to deliver power. The power supply level can be adjusted by the user until the RX power level is sufficiently high to power the NI device at the maximum expected operating distance. The user can modify the setting in a list of constants in the code, or by using push buttons on the MCU board. When increasing power level, the local and the whole-body SAR levels must be examined in order to avoid causing excessive heating in the subjects, as detailed in the next section.

Fig. 15 shows the simultaneously measured levels of the impedance sensing voltage, V_{SENSE}, and the transmitted DC power levels (with the LED in series with the load). The impedance indicator (V_{SENSE}) drops distinctly by more than 20 mV which is readily detectable by the load-tracking algorithm beyond the common sensing errors. The sensing voltage does not rapidly drop once the receiver is turned on. This is because the supply current decreases simultaneously with the

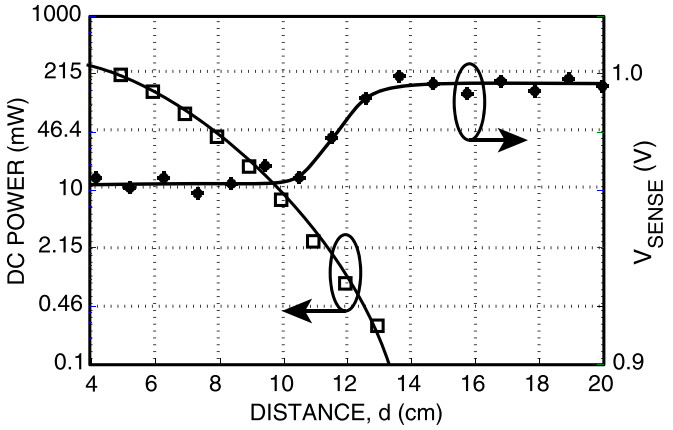

Fig. 15. Experimentally measured transferred power level at the receiver (with the LED connected) at 4 cm–20 cm vertical distances from the TX. The output of the sensing amplifier (V_{SENSE}) is also shown. V_{SENSE} drop caused by the receiver is detectable by the microcontroller below 11 cm distance.

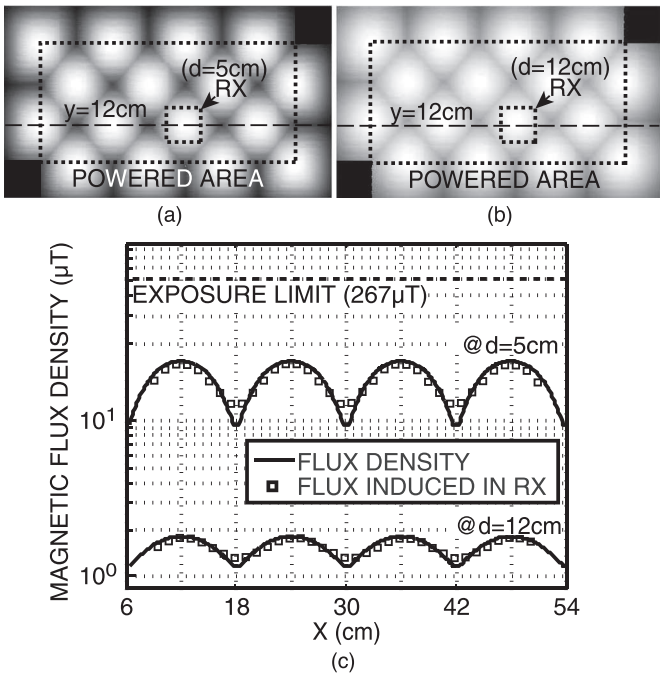

Fig. 16. Experimentally measured magnetic flux coverage above the inductive powering floor at (a) 5 cm and (b) 12 cm above the cage floor. The coverage is more uniform at the farther distance as the weaker flux regions (dead zones) are diminished. (c) The cross-section of the experimentally measured magnetic flux density at $\mathrm{d} = 5$ cm and $\mathrm{d} = 12$ cm above, and along the $\mathrm{y} = 12$ cm line across the floor. Because of the spatial averaging (over the 4 cm $\times$ 4 cm RX area), the total magnetic flux induced into the RX varies more slowly across the floor than the value of flux density. This further diminishes the impact of the dead zones seen in the flux density graphs [solid lines as well as the maps in (a) and (b)]. The average magnetic flux density is measured by placing the RX coil over the TX coil array while the voltage induced in the open-circuited RX coil is recorded.

increase in the reflected impedance [R_{EQ2} in Fig. 7(b)] as the receiver approaches the transmitter in Fig. 15.

F. Magnetic Field Distribution

The measured coverage of the magnetic flux density is plotted in Fig. 16 at distances 5 cm and 12 cm from the floor, verifying the compliance of the near-field system with the regulated levels of magnetic field intensity. As evident from the flux density levels in Fig. 16(a), there are points on the XY plane at 5 cm distance where the magnetic field is significantly weaker (troughs), which are the bordering points among each of the four adjacent coils. However, farther away from the floor, the weak point are diminished as shown in Fig. 16(b) (at $\mathrm{d} = 12$ cm). The reduced sensitivity of RX placement on the XY plane at further separation distances is helpful as it in fact evens out the flux distribution where its average value is most limited. Fig. 16(c) shows the 2D cross-section plots of the magnetic flux density over the floor along the $\mathrm{y} = 12$ cm line. It can be seen that the field strength is significantly more uniform at $\mathrm{d} = 12$ cm [Fig. 16(b)] than at $\mathrm{d} = 5$ cm [Fig. 16(a)] even though it is weaker at $\mathrm{d} = 12$ cm.

The non-uniform field distribution closer to the floor can be tolerated as the minimum field intensity (in the troughs) is still significantly higher than the minimum operable value for the RX. The minimum operable value is the minimum field strength that can sufficiently power the RX and sustain the operation of the microsystem. The cross-section plot in Fig. 16(c) also shows the variation of the average flux over the 4 cm $\times$ 4 cm area of the receiver which is the actual impact of the field variations on the harvested power. As evident, the variations of the induced flux is less than that of the instantaneous flux levels which further diminishes the negative impact of the flux troughs. The maximum operating distance of 11 cm is determined as the farthest operating distance from where sufficient power can be recovered at the weakest flux density trough.

G. Other Power Delivery Factors

1) Load Impedance Variation: The measured values of the received DC power which are plotted in Fig. 14 are based on a 3.3 kΩ resistive load (R_L) connected on the receiver board as shown in Fig. 6(b). This plot represents the peak current consumption of the microsystem powered by the RX. The actual current consumption is likely to be less than this value, resulting in a higher load impedance and a resistive mismatch. However, since the load voltage only increases in this scenario, the resistive mismatch caused by the RX approaching the floor does not decrease the delivered power or disrupt power delivery.

2) Resonance Frequency Variations: Each of the TX coils in the array are individually tuned to their resonance frequency during the calibration phase at the system startup. As a result, there is a slight change in the operating frequency as the animal moves from one TX coil to the next. This causes a small mismatch between the reactance of the RX coil and the RX capacitor C_{RX} in Fig. 6(b). Based on the measurement data in Fig. 17(a), the reactive mismatch in the RX reduces the power delivery by approximately 5%, which must be accounted for when setting up the floor power level. A dynamic impedance matching algorithm (in the microsystem) may offset this power loss, depending on the power overhead to run the algorithm.

3) Tilting and Angular Misalignment: The RX board is mounted on the back of the animal such that the RX remains parallel to the floor. However, there are times when the animal tilts to one side or lowers its head, in which cases the RX may no longer remain parallel to the floor. Since the floor power is high enough to keep the RX fully powered when the

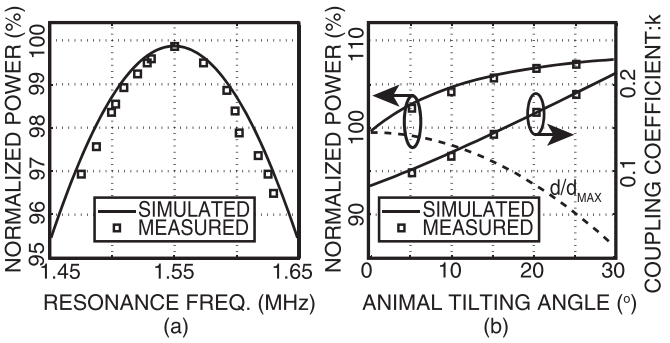

Fig. 17. Relative changes in the level of delivered power due to (a) resonance frequency variation among coils in the array, and (b) RX angular misalignment caused by animal tilting to one side. $\mathbf{d/d_{MAX}}$ is the distance from center of the RX at the tilting angle normalized to the maximum expected distance $\mathbf{d_{MAX}}$.

animal stretches its back all the way upward, the misalignments caused by lowering the RX on one side does not disrupt power delivery. This is because the drop in k due to the resulting angular misalignment is outweighed by a simultaneous rise in the coupling coefficient k due to the RX center moving closer to the floor. Fig. 17(b) shows the variations in the received power due to angular misalignments caused by tilting of the animal to one side. The power delivered to the RX remains sufficient at all times. It must be noted that, similar to the power delivery, the load detection is also uninterrupted by the tilting of the animal as described by Fig. 17(b). This is because the reflected impedance in Fig. 7(b) (R_{EQ2}) is only diminished when the coupling coefficient k is reduced. This however, as shown in Fig. 17(b), is not the case when the animal tilts during the experiment.

H. Design Comparisons

Measured characteristics of the developed SAR-constrained inductive powering system and of similar recently reported designs are listed in Table I. The performance of all powering systems is evaluated at their reported nominal operating distance. For appropriate comparison of power transfer metrics, the separation distance at which the power transfer is measured is selected proportionately to the outer diameter of the transmitting coil (this ratio is also used in the FOM reported by [32] and [20]). Therefore, the performance of the developed system is listed for the separation distance of 8 cm which results in approximately the same size-to-separation (70%) ratio as the designs in [14], [21]. While it provides slightly less coil-to-coil efficiency than other reported works in Table I, the system is capable of transferring more power by creating more magnetic flux density at the receiver than other reported work as shown in Table I. This is due to the higher limit on non-ionizing field exposure (10.9 A/m) at the selected operating frequency of 1.5 MHz as compared with the lower limit of 1.2 A/m at the conventionally used operating frequency of 13.6 MHz. While the power efficiency is mostly affected by the receiver size-to-coil separation ratio, the maximum deliverable power is determined exclusively by the operating frequency and the size of the receiving coil.

TABLE I
PERFORMANCE SUMMARY AND COMPARISON

Reference	[14]	[33]	[20]	[29]	[21]	[32]	This work
Frequency (f_o)(MHz)	13.65	8	13.6	2.457	13.56	160	1.5
Exposure limit @f_o(A/m)*	1.2	2.04	1.2	6.63	1.2	0.073	10.9
Distance (cm)	12	7	4	4	7	1	8, 11†
Coupling (k)	0.035	0.069	0.063	0.004‡	-	-	0.15
Load (R_L)(kΩ)	0.5	1	0.1	-	600	150	3.3
Transferred Power (mW)	20-145	10	100	1.7	24	1	21-225
TX Parameters							
Size (OD_1)(cm)	16.6	4.3	13.5	20×15	17	1.45	11.5
Turns (N_1)	2	15	3	22	1	2	5
Copper weight (g)	3.3	0.41	192	1.35	31.88	0.064	3.4
Inductance (L_1) (μH)	0.68	5.07	1.68	500‡	0.716	0.05	10.62
Quality factor	166	113	286	-	150	-	127
Capacitance (C_{TX})(pF)	203	78	82	8.4‡	191	19	1050
RX Parameters							
Size (OD_2)(cm)	4	1	4.4	1.9	2.5	5	4
Turns (N_2)	4	6	3	82	2	2	22
Copper weight (g)	1.4	0.01	0.91	0.21‡	0.573	8×10^{-5}	0 .44
Fill factor (%)	-	28	2	58	-	32	88
Inductance (L_2)(μ H)	1.25	0.45	0.8	80‡	0.48	0.06	10.35
Quality factor	177	21.7	150	-	136	11.05	74
Capacitance (C_{RX})(pF)	123	880	171	52‡	285	9.14	1043
Performance							
Coil-to-coil efficiency (η_{COIL})(%)	42	54.8	69	**10**	29	1.4	39
Maximum deliverable power (P_{max})(W)	1.13	0.0057	2.8	0.65	1.13	0.00021	15.9

*Based on *IEEE Standard C95.1-1991*.

†Nominal distance 8 cm, and maximum distance 11 cm.

‡Estimated based on available parameters.

- Specification not available.

Table II shows the scalability of the developed inductive powering system in terms of the type and the quantity of the components required for each scaling unit (one four-coil TX tile). It can be seen that by implementing load tracking and location sensing with only an impedance sensing circuit, this design saves on components such as magnetic sensors and RFID readers. Moreover, individual frequency generation circuits on each board (as done in [14]) have been replaced here by a single clock generator on the controller board. While simultaneously more than one coil can be driven by the clock signal in this design, the coils cannot be individually tuned in such a scenario (have different resonant frequencies). This could be an advantage of having separate frequency generation circuits on each driver board. However, given the lower operating frequency in this design, the resonance points of each coil will be much more predictable as the parasitic capacitance of the TX coils are negligible compared to the value of C_{TX} (as shown in Fig. 6). Therefore, the exact value of C_{TX} can be selected such that all the TX coils resonate at the same frequency, and can be driven with the same clock signal. Simultaneously driving multiple coils, of course, increases the magnetic field level.

Table II shows that by eliminating the need for multiple MCUs, RFID readers, Ethernet-to-serial ports, and magnetic sensors, the proposed system offers greater scalability at a lower cost. The current-sensing feedback simplifies dynamic

TABLE II
DESIGN SCALABILITY AND COST CONSIDERATIONS

Reference	[14]	This work
Location-sensing method	3D Magnetic Sensors (×N*)	Reflected impedance (software implementation)
Power control mechanism	RFID Readers (×N)	Reflected impedance (software implementation)
Serial interface with drivers	Ethernet devices (×N)	I^2C buffers (×N)
# of Sig. gen.	N	1
# of MPU's	N/3	1
Coil material	4-layer PCB	2-layer PCB

*N is the number of TX coils.

tuning and enables load-tracking at no additional cost for every new tile. Additional tiles can be scanned by the impedance sensing circuit in the driver board at the same time as they are being powered. However, since all the TX coils are scanned by one MCU, one scaling limitation is the increased execution length of the calibration and global search algorithms as the MCU must scan though all the additional TX coils. However, the calibration routine runs only once at the startup and the impedance scores are available as long as the RAM content is preserved. Therefore, in a very large coil array the calibration routine can be skipped as long as the scores are available at the startup. The global search, on the other hand, must still be performed every time the tracking routine fails which could take an impractically long time in a system with far too many TX coils. To shorten the search for the load, the global search must then be replaced by a series of successively farther-reaching localized searches until the load is located. In other words, if the load cannot be located among the most immediate neighboring TX coils, the algorithm must begin scanning at a radius of one more TX coil away from the last known position of the load and continue until the RX is located.

I. In Vivo Power Transfer Validation

The cellular inductive powering system was validated *in vivo* in a freely moving rat experiment. All the experimental procedures were conducted at the Hospital for Sick Children (Toronto) and performed according to the protocols approved by the Animal Care and Ethic Committee. One Wistar rat (250 g, male) underwent general anesthesia.

The hair on the head (area: 10 mm × 10 mm) and back (area: 15 mm× 15 mm) was trimmed. A multi-channel neural amplifier and stimulator device [34] and the inductive power receiver coil PCB were mounted using adhesive PDMS on the head and the back, respectively.

After a short recovery period, the animal was placed in the cage shown in Fig. 18(a). The cage was placed on the overlapping area of the two coil layers [same as outlined in Figs. 4(b), 16(a) and (b)]. The inductive powering system was turned on underneath the cage while a video camera recorded the experiment. As shown in Fig. 18(b) and (c), a solid lit LED on the RX board mounted on the back of the animal indicated continuous power transfer to the board as the animal moved around in its cage. The minimum 2.5 mA current required to turn on the LED is an indication of a rectified 10 V voltage being delivered across the load and the LED. In the case of a sudden movement, the LED began flashing indicating that the local tracking algorithm has aborted and the MCU has begun performing global search. The LED became solid again within a fraction of a second which indicated that the MCU had found the new location of the animal. A supercapacitor in the microsystem bridges any such supply interruptions. The power delivery performance of the system was evaluated while the rat was exploring the cage, grooming in different positions, eating from the floor, or while drinking water; the LED only briefly flashes after a sudden movement and stays solid in all other scenarios.

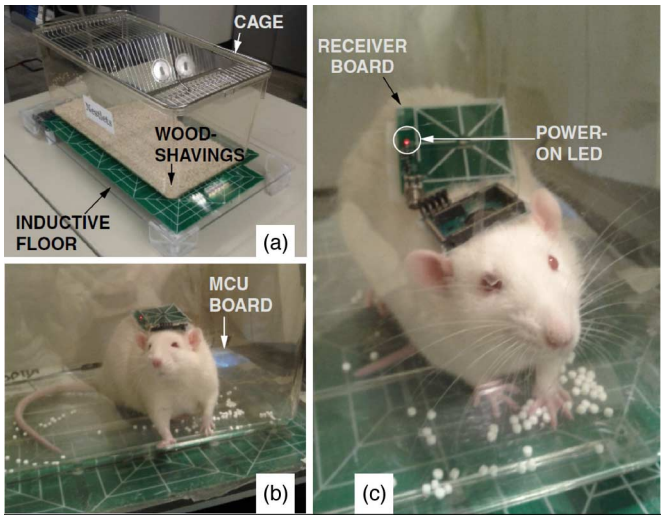

Fig. 18. (a) Rodent cage covering the overlapping region of the 2 layers of the transmitting arrays. (b) Receiver on a white Wistar rat being powered while animal is lying down anesthetized (the LED indicates power transfer). (c) Power transfer when animal is awake and standing up.

V. CONCLUSION

A practical inductive power transfer system for mobile neural interface devices featuring a dynamic load tracking technology and reduced non-ionizing radiation levels has been designed, prototyped and tested. The developed system was shown to transfer sufficiently high levels of inductive power with the smallest reported levels of non-ionizing radiation through the tissue and in the vicinity of the coils.

REFERENCES

[1] H. Kassiri, A. Bagheri, N. Soltani, K. Abdelhalim, H. Jafari, M. T. Salam, J. L. P. Velazquez, and R. Genov, "Inductively-powered direct-coupled 64-channel chopper-stabilized epilepsy-responsive neurostimulator with digital offset cancellation and tri-band radio," in *Proc. IEEE Eur. Solid-State Circuits Conf.*, Venice, Italy, Sep. 2014.

[2] K. Deisseroth, "Optogenetics," *Nature Methods*, vol. 8, no. 1, pp. 26–29, 2011.

[3] A. Aravanis, L. Wang, F. Zhang, L. Meltzer, Z. Mogri, B. Schneider, and K. Deisseroth, "An optical neural interface: In vivo control of rodent motor cortex with integrated fiberoptic and optogenetic technology," *J. Neural Eng.*, vol. 4, no. 3, pp. 143–156, 2007.

[4] J. Weiland, A. Cho, and M. Humayun, "Retinal prostheses: Current clinical results and future needs," *Ophthalmology*, vol. 118, no. 11, pp. 2227–2237.

[5] B. Eversmann, M. Jenkner, F. Hofmann, R. Brederlow, P. Fromherz, F. Brenner, M. Schreiter, R. Gabl, K. Plehnert, M. Steinhauser, G. Eckstein, D. Schmitt-Landsiedel, and R. Thewes, "A 128 × 128 CMOS biosensor array for extracellular recording of neural activity," *IEEE J. Solid-State Circuits*, vol. 38, no. 12, pp. 2306–2317, 2003.

[6] R. Normann, E. Maynard, P. Rousche, and D. Warren, "A neural interface for a cortical vision prosthesis," *Vis. Res.*, vol. 39, no. 15, pp. 2577–2587, 1999.

[7] K. Abdelhalim, L. Kokarovtseva, J. Perez Velazquez, and R. Genov, "915-MHz FSK/OOK wireless neural recording SoC with 64 mixed-signal FIR filters," *IEEE J. Solid-State Circuits*, no. 99, pp. 1–16, 2013.

[8] H.-M. Lee and M. Ghovanloo, "A power-efficient wireless capacitor charging system through an inductive link," *IEEE Trans. Circuits Syst. II, Exp. Briefs*, vol. 60, no. 10, pp. 707–711, Oct. 2013.

[9] T. Szuts, V. Fadeyev, S. Kachiguine, A. Sher, M. Grivich, and M. Agrocho, "A wireless multi-channel neural amplifier for freely moving animals," *Nature Neurosci.*, vol. 14, no. 2, pp. 263–269, 2011.

[10] Y. Zhu, S. Wang, M. Li, and C. Wu, "Studying on gnawing testing method of rodent-proof wire and cable," in *Proc. Int. Symp. Electrical Insulating Materials*, 2008, pp. 334–337.

[11] A. Schwartz, X. Cui, D. Weber, and D. Moran, "Brain-controlled interfaces: Movement restoration with neural prosthetics," in *Proc. IEEE/ICCME Int. Conf. Complex Medical Engineering*, 2010, pp. 79–84.

[12] D. Budgett, A. Hu, P. Si, W. Pallas, M. Donnelly, J. Broad, C. Barrett, S. Guild, and S. Malpas, "Novel technology for the provision of power to implantable physiological devices," *J. Appl. Phys.*, vol. 102, no. 4, pp. 1658–1663, 2007.

[13] A. Bagheri, S. Gabran, M. Salam, J. Perez Velazquez, R. Mansour, M. Salama, and R. Genov, "Massively-parallel neuromonitoring and neurostimulation rodent headset with nanotextured flexible microelectrodes," *IEEE Trans. Biomed. Circuits Syst.*, vol. 7, no. 5, pp. 601–609, Oct. 2013.

[14] U. Jow, P. McMenamin, M. Kiani, J. R. Manns, and M. Ghovanloo, "EnerCage: A smart experimental arena with scalable architecture for behavioral experiments," *IEEE Trans. Biomed. Eng.*, vol. 61, no. 1, Jan. 2014.

[15] S. Mirbozorgi, H. Bahrami, M. Sawan, and B. Gosselin, "A smart multicoil inductively coupled array for wireless power transmission," *IEEE Trans. Ind. Electron.*, vol. 61, no. 11, pp. 6061–6070, 2014.

[16] K. M. Silay, C. Dehollain, and M. A. Declercq, "Closed-loop remote powering link for wireless cortical implants," *IEEE Sens. J.*, vol. 13, no. 9, pp. 3226–3235, 2013.

[17] E. Kilinc, G. Conus, C. Weber, B. Kawkabani, F. Maloberti, and C. Dehollain, "A system for wireless power transfer of micro-systems in-vivo implantable in freely moving animals," *IEEE Sens. J.*, vol. 14, no. 2, pp. 522–531, 2014.

[18] C. T. Wentz, J. G. Bernstein, P. Monahan, A. Guerra, A. Rodriguez, and E. S. Boyden, "A wirelessly powered and controlled device for optical neural control of freely-behaving animals," *J. Neural Eng.*, vol. 8, no. 4, pp. 0460210–46021, Jun. 2011.

[19] T. Sekitani, M. Takamiya, Y. Noguchi, S. Nakano, Y. Kato, T. Sakurai, and T. Someya, "A large-area wireless power-transmission sheet using printed organic transistors and plastic MEMS switches," *Nature Mater.*, vol. 6, no. 6, pp. 413–417, 2007.

[20] S. Mirbozorgi, H. Bahrami, M. Sawan, and B. Gosselin, "A smart cage with uniform wireless power distribution in 3D for enabling long-term experiments with freely moving animals," *IEEE Trans. Biomed. Circuits Syst.*., 2015, IEEE Xplore website, Early Access paper.

[21] B. Lee, M. Kiani, and M. Ghoovanloo, "A smart wirelessly-powered homecage for long-term high-throughput behavioral experiments," *IEEE Sens. J.*, vol. 15, no. 9, Sep. 2015.

[22] J. Mur-Miranda, G. Fanti, Y. Feng, K. Omanakuttan, R. Ongie, A. Setjoadi, and N. Sharpe, "Wireless power transfer using weakly coupled magnetostatic resonators," in *Proc. IEEE Energy Conversion Congress and Exp.*, 2010, pp. 4179–4186.

[23] *Standard for Safety Levels With Respect to Human Exposure to Radio Frequency Electromagnetic Fields, 3 kHz to 300 GHz*, IEEE Std C95. 1-2005 (Revision of IEEE Std C95.1-1991), 2006.

[24] J. Gordon, "Effects of ambient temperature and exposure to 2450-MHz microwave radiation on evaporative heat loss in the mouse," *J. Microw. Power*, vol. 17, pp. 145–150, 1982, IEEE-651.

[25] J. Gordon, "Note: Further evidence of an inverse relation between mammalian body mass and sensitivity to radio-frequency electromagnetic radiation," *J. Microw. Power*, vol. 18, pp. 377–383, 1983.

[26] A. Guy, P. Kramar, C. Harris, and C. Chou, "Long-term 2450-MHz CW microwave irradiation of rabbits: Methodology and evaluation of ocular and physiologic effects," *J. Microw. Power*, vol. 15, pp. 37–44, 1980, [IEEE-654].

[27] N. Soltani, M. S. Aliroteh, and R. Genov, "Cellular inductive powering system for weakly-linked resonant rodent implants," in *Proc. IEEE Biomedical Circuits and Systems. Conf.*, Rotterdam, Netherlands, Oct. 2013.

[28] U. Jow and M. Ghovanloo, "Design and optimization of printed spiral coils for efficient transcutaneous inductive power transmission," *IEEE Trans. Biomed. Circuits Syst.*, vol. 1, no. 3, pp. 193–202, Sep. 2007.

[29] K. Eom, J. Jeong, T. Lee, J. Kim, J. Kim, S. Lee, and S. Kim, "A wireless power transmission system for implantable devices in freely moving rodents," *Med. Biol. Eng. Comput.*, vol. 52, no. 8, pp. 639–651, Aug. 2014.

[30] M. Ghovanloo and S. Atluri, "A wide-band power-efficient inductive wireless link for implantable microelectronic devices using multiple carriers," *IEEE Trans. Circuits Syst. I, Reg. Papers*, vol. 54, no. 10, pp. 2211–2221, Oct. 2007.

[31] M. Zargham and P. Gulak, "Maximum achievable efficiency in near-field coupled power-transfer systems," *IEEE Trans. Biomed. Circuits Syst.*, vol. 6, no. 3, pp. 228–245, Jun. 2012.

[32] M. Zargham and P. Gulak, "Fully integrated on-chip coil in 0.13 CMOS for wireless power transfer through biological media," *IEEE Trans. Biomed. Circuits Syst.*, vol. 9, no. 2, pp. 259–271, Apr. 2015.

[33] K. M. Silay, C. Dehollain, and M. Declercq, "Inductive power link for a wireless cortical implant with two-body packaging," *IEEE Sensors J.*, vol. 11, no. 11, pp. 2825–2833, Nov. 2011.

[34] A. Bagheri, S. R. I. Gabran, M. T. Salam, J. L. Perez Velazquez, R. R. Mansour, M. M. A. Salama, and R. Genov, "Massively-parallel neuromonitoring and neurostimulation rodent headset with nanotextured flexible microelectrodes," *IEEE Trans. Biomed. Circuits Syst.*, vol. 7, no. 5, pp. 601–609, Oct. 2013.

[35] C. Qian, J. Parramon, and E. and Sanchez-Sinencio, "A micropower low-noise neural recording front-end circuit for epileptic seizure detection," *IEEE J. Solid-State Circuits*, vol. 46, no. 6, pp. 1392–1405, 2011.

[36] D. McCormick, A. Hu, P. Nielsen, S. Malpas, and D. Budgett, "Powering implantable telemetry devices from localized magnetic fields," in *Proc. Annu. Int. Conf. Engineering in Medicine and Biology Soc.*, 2007, pp. 2331–2335.

[37] A. Kurs, A. Karalis, R. Moffatt, J. Joannopoulos, P. Fisher, and M. Soljai, "Wireless power transfer via strongly coupled magnetic resonances," *Science*, no. 317, pp. 83–86, 2007.

[38] N. Soltani and F. Yuan, "A high-gain power-matching technique for efficient radio-frequency power harvest of passive wireless microsystems," *IEEE Trans. Circuits Syst. I, Reg. Papers*, vol. 57, no. 10, pp. 2685–2695.

[39] K. Abdelhalim, V. Smolyakov, and R. Genov, "A phase synchronization and magnitude processor VLSI architecture for adaptive neural stimulation," in *Proc. IEEE Biomedical Circuits and Systems Conf.*, 2010, pp. 5–8.

[40] R. Harrison, "Designing efficient inductive power links for implantable devices," in *Proc. IEEE ISCAS*, Jun. 2007, pp. 2080–2083.

[41] Z. Low, R. Chinga, R. Tseng, and J. Lin, "Design and test of a high-power high-efficiency loosely coupled planar wireless power transfer system," *IEEE Trans. Ind. Electron.*, vol. 56, no. 5, pp. 1801–1812, 2009.

[42] S. Kim, R. Bhandari, M. Klein, S. Negi, L. Rieth, P. Tathireddy, M. Toepper, H. Oppermann, and F. Solzbacher, "Integrated wireless neural interface based on the Utah electrode array," *Biomed. Microdev.*, vol. 11, no. 2, pp. 453–466, 2009.

[43] B. Lenaerts and R. Puers, "An inductive power link for a wireless endoscope," *Biosens. Bioelectron.*, vol. 22, no. 7, pp. 1390–1395, 2007.

[44] F. Mounaim and M. Sawan, "Integrated high-voltage inductive power and data-recovery front end dedicated to implantable devices," *IEEE Trans. Biomed. Circuits Syst.*, vol. 5, no. 3, pp. 283–291, Jun. 2011.

[45] S. Ayazian, V. Akhavan, E. Soenen, and A. Hassibi, "A photovoltaic-driven and energy-autonomous CMOS implantable sensor," *IEEE Trans. Biomed. Circuits Syst.*, vol. 6, no. 4, pp. 336–343, Aug. 2012.

[46] H. Ko and P. Feng, "Biomedical implantable systemshistory, design, trends," in *Implantable Bioelectronics*. Boca Raton, FL, USA: CRC Press, 2014.

[47] A. Shameli, A. Safarian, A. Rofougaran, M. Rofougaran, J. Castaneda, and F. D. Flaviis, "A UHF near-eld RFID system with fully integrated transponder," *IEEE Trans. Microw. Theory Tech.*, vol. 56, no. 5, pp. 1267–1277, May 2008.

Nima Soltani (S'13) received the B.Eng. and M.A.Sc. degrees in electrical engineering from Ryerson University, Toronto, ON, Canada, in 2007 and 2010, respectively.

Currently, he is working toward the Ph.D. degree at the University of Toronto, Toronto, ON, Canada. His M.A.Sc. thesis focused on ultralow-power RF circuits for passive microsystems, and RF power transmission. From 2010 to 2011, he worked at Solace Power Inc. on the development of the first electrical induction system for medium-range wireless power transfer. His doctoral dissertation focuses on inductively-powered implantable brain chemistry monitoring systems. He is a cofounder of BrainCom Inc., a Toronto-based company specializing in the development of wearable and implantable platforms for high-resolution brain signal processing and acquisition.

Miaad S. Aliroteh (S'13) received the B.A.Sc. degree (with honors) in engineering science with a major in electrical and computer engineering from the University of Toronto, Toronto, ON, Canada, in 2012.

Currently, he is working toward the Ph.D. degree in electrical engineering at Stanford University, Stanford, CA, USA. His research interests include multimodal biomedical imaging, biometrics, biosensing and diagnostics, lab-on-a-chip, neural interfaces, neuroprostheses, wireless implantable or wearable biomedical devices, and analog and RF VLSI.

Mr. Aliroteh was awarded the PGS M scholarship from the the Natural Sciences and Engineering Research Council of Canada in 2012 and the Qualcomm Innovation Fellowship in 2014.

M. Tariqus Salam (M'09) received the B.Sc. degree in electrical and electronics engineering from the Islamic University of Technology, Gazipur, Bangladesh, the M.A.Sc. degree in electrical and computer engineering from Concordia University, Montreal, QC, Canada, and the Ph.D. degree in electrical engineering from Ecole Polytechnique de Montreal, Montreal, QC, Canada, in 2003, 2007, and 2012, respectively.

He finished his first postdoctoral training in the Intelligent Sensory Microsystems Laboratory and Hospital for Sick Children Hospital. Currently, he is in his second Postdoctoral Fellowship at Toronto Western Hospital with an industrial partner. His specific research interests are in the areas of low-power circuit design, brain-machine interface, and mental disease diagnosis and closed-loop therapy.

Jose Luis Perez Velazquez was born in Zaragoza, Spain. He received the degree of Licenciado in chemistry (Biochemistry, Universities of Zaragoza and Complutense of Madrid), and the Ph.D. degree from the Department of Molecular Physiology and Biophysics, Baylor College of Medicine, Houston, TX, USA, in 1992, and homologated to Doctorate in Chemistry by the Spanish Ministry of Culture in 1997.

Currently, he is an Associate Scientist in the Neuroscience and Mental Programme and the Brain and Behaviour Center at the Hospital For Sick Children, Toronto, ON, Canada, and Associate Professor at the University of Toronto, Toronto, ON, Canada.

Roman Genov (S'96–M'02–SM'11) received the B.S. degree in electrical engineering from the Rochester Institute of Technology, NY, USA, in 1996, and the M.S.E. and Ph.D. degrees in electrical and computer engineering from Johns Hopkins University, Baltimore, MD, USA, in 1998 and 2003, respectively.

Currently, he is a Professor in the Department of Electrical and Computer Engineering at the University of Toronto, Toronto, ON, Canada, where he is a member of the Electronics Group and Biomedical Engineering Group and the Director of Intelligent Sensory Microsystems Laboratory. His research interests are primarily in analog integrated circuits and systems for energy-constrained biological, medical, and consumer sensory applications.

Dr. Genov was a corecipient of the Best Paper Award of IEEE Biomedical Circuits and Systems Conference, Best Student Paper Award of the IEEE International Symposium on Circuits and Systems, Best Paper Award of the IEEE Circuits and Systems Society Sensory Systems Technical Committee, Brian L. Barge Award for Excellence in Microsystems Integration, MEMSCAP Microsystems Design Award, DALSA Corporation Award for Excellence in Microsystems Innovation, and Canadian Institutes of Health Research Next Generation Award. He was a Technical Program Cochair at the IEEE Biomedical Circuits and Systems Conference. He was an Associate Editor of IEEE TRANSACTIONS ON CIRCUITS AND SYSTEMS—II: EXPRESS BRIEFS and IEEE SIGNAL PROCESSING LETTERS. Currently, he is an Associate Editor of IEEE TRANSACTIONS ON BIOMEDICAL CIRCUITS AND SYSTEMS and a member of the IEEE International Solid-State Circuits Conference International Program Committee.